1 **Large-scale voltage imaging in the brain using targeted illumination**

2

3

4 *Sheng Xiao[1*], Eric Lowet[1*], Howard J. Gritton[1,2*], Pierre Fabris[1], Yangyang Wang[1], Jack*

5 *Sherman[1], Rebecca Mount[1], Hua-an Tseng[1], Heng-Ye Man,[3] Jerome Mertz[1] and Xue Han[1#]*

6 *[1]Boston University, Department of Biomedical Engineering, Boston, MA 02215*

7 *[2]Department of Comparative Biosciences, University of Illinois, Urbana, IL 61802*

8 *[3]Boston University, Department of Biology, Boston, MA 02215*

9

10

11 *These authors contributed equally.

12 #Correspondence: xuehan@bu.edu

13

14 **Keywords:** Optical Imaging, voltage sensors, plasma membrane voltage, spikes,

15 electrophysiology, coherence, epi-fluorescence microscopy

16

17

18

19 **Abstract**

20 Recent improvements in genetically encoded voltage indicators enabled high precision imaging

21 of single neuron's action potentials and subthreshold membrane voltage dynamics in the

22 mammalian brain. To perform high speed voltage imaging, widefield microscopy remains an

23 essential tool to record activity from many neurons simultaneously over a large anatomical area.

24 However, the lack of optical sectioning makes widefield microscopy prone to background signal

25 contamination. We implemented a simple, low cost, targeted illumination strategy based on a

26 digital micromirror device (DMD) to restrict illumination to the cells of interest to improve

27 background rejection, and quantified optical voltage signal improvement in neurons expressing

28 the fully genetically encoded voltage indicator SomArchon. We found that targeted illumination,

29 in comparison to widefield illumination, increased SomArchon signal contrast and reduced

30 background cross-contamination in the brains of awake mice. Such improvement permitted the

31 reduction of illumination intensity, and thus reduced fluorescence photobleaching and prolonged

32 imaging duration. When coupled with a high-speed sCMOS camera, we routinely imaged tens of

33 spiking neurons simultaneously over several minutes in the brain. Thus, the DMD-based targeted

34 illumination strategy described here offers a simple solution for high-speed voltage imaging

35 analysis of large scale network at the millisecond time scale with single cell resolution in the brains

36 of behaving animals.

Introduction

38 Recent advances in genetically encoded voltage indicators (GEVIs) have enabled neuroscientists
39 to directly measure membrane voltage from individual neurons in the mammalian brains [1–6]. In
40 particular, a few recent GEVIs, including SomArchon, QuasAr3, Voltron, ASAP3 and Ace2N, have
41 achieved sufficient sensitivity to capture individual action potentials from single neurons in
42 behaving mice. Of these high performance GEVIs, several are fully genetically encoded, whereas
43 others are hybrid sensors that require exogenous chemicals [8–14, 17]. One class of fully genetically
44 encoded indicators detects voltage dependent fluorescence of fluorophores fused to voltage
45 sensitive peptide domains derived from voltage gated ion channels, voltage sensitive
46 phosphatases or rhodopsins [8–14]. For these GEVI designs, changes in plasma membrane voltage
47 induce confirmational transitions of the voltage sensitive domains, which subsequently alter the
48 absolute fluorescence intensity or the efficiency of Forster resonance energy transfer of the
49 tethered fluorophores. A recent example is ASAP3 that measures voltage dependent fluorescence
50 of a circular permutated GFP fused to the voltage sensing domain of G. gallus voltage-sensing
51 phosphatase[4]. Another class of fully genetically encoded indicators is single compartment and
52 directly detects the intrinsic voltage dependent fluorescence of engineered rhodopsins, such as
53 QuarsAR3, Archon and SomArchon [3,5,15]. To improve fluorescence signals, bright chemical
54 fluorophores have also been explored in the design of GVEIs, yielding a class of high-performance
55 hybrid GEVIs that requires both exogeneous chemical dyes and the corresponding voltage sensing
56 protein counterparts[2,16,17].

57

58 With rapid and continued improvements of GEVIs, voltage imaging offers great promise for direct
59 analysis of neuronal voltage dynamics in the brain. To capture fast membrane voltage
60 fluctuations, especially action potentials that occur on the millisecond and sub-millisecond time
61 scale, fluorescence voltage imaging needs to be performed at a near kilohertz sampling speed.
62 Point scanning techniques, such as multiphoton microscopy, have minimum signal cross-
63 contamination and out-of-focus background due to confined excitation volumes[18], but are
64 generally limited to video-rate acquisition speed due to the use of mechanical scanners. Fast
65 random access scanning using acousto-optic deflectors has been demonstrated with kilohertz
66 sampling rates[4], though these devices require a complicated setup, are sensitive to motion
67 artifacts, and more importantly, can only record very few pre-selected cells at once. More
68 recently, kilohertz frame rate two-photon imaging over a field-of-view (FOV) of $50 \times 250 \ \mu m^2$ has
69 been demonstrated by means of passive pulse splitting from a specialized low-repetition rate
70 laser[19]. However, its stringent alignment requirements, high cost, and concerns regarding long-
71 term system stability remain a major obstacle for its widespread use for neuroscience studies.

72

73 Alternatively, widefield microscopy, especially when equipped with the newly developed high-
74 speed large-area sCMOS cameras, remains a cost-effective and easily implementable solution for
75 wide FOV, kilohertz frame-rate imaging. This ability to image a large FOV at high spatiotemporal
76 resolution is particularly critical to resolving morphological details of individual neurons, and to
77 correct for tissue movement associated with physiological processes (i.e., heart rate, breathing)
78 that are unavoidable when imaging the brains of awake behaving animals. However, a major
79 limitation of widefield microscopy is the inability to reject out-of-focus and scattered light[20],
80 making it prone to signal contamination and background shot noise caused by non-specific
81 excitations[21]. To address this problem molecularly, recently developed GEVIs have utilized soma

82 targeting peptides[22], such as the axon initial segment targeting motif of the potassium channel
83 Kv2.1, which successfully restrict the expression of GEVIs to soma or proximal dendrites. For
84 example, SomArchon, QuasAr3, Voltron, and ASAP3-kv all include such soma targeting motifs,
85 which are critical for their success in measuring membrane voltage in the brains of behaving
86 animals, using widefield or two-photon microscopes [2–6]. Restricting the expression of GEVIs to a
87 sparse subset of neurons can also help reduce background signal contamination, and this strategy
88 was recently used to achieve simultaneous imaging of tens of neurons using the hybrid sensor
89 Voltron[2].

90

91 In parallel with molecular targeting of GEVIs, targeted illumination in optical microscopy design
92 has been proposed as a simple strategy to improve upon a widefield microscopy for enhancing
93 image contrast and improving signal-to-noise ratio (SNR)[23]. For example, by targeting illumination
94 to cell bodies or plasma membranes, voltage imaging performance has been significantly
95 improved[4-6]. However, limited by the attainable FOV and weak GEVI fluorescence contrast,
96 voltage imaging in the intact brain has largely been limited to simultaneous sampling of few cells.
97 To reduce out-of-focus light, and to improve voltage imaging performance, we integrated a
98 simple, low cost, targeted illumination strategy into a standard widefield microscope, where a
99 digital micromirror device (DMD) was used to restrict the illumination light to specific neurons of
100 interest. We directly compared SomArchon imaging performance of the same neurons under
101 targeted versus widefield illumination, in both cultured neuron preparations, and from the brains
102 of awake behaving mice. We found that illumination targeting reduced nonspecific background
103 fluorescence and fluorescence signal cross-contamination, leading to increased SomArchon spike
104 signal-to-background ratio. The improvement of SomArchon fluorescence contrast allows us to
105 decrease the total excitation power over the FOV that reduces fluorescence photobleaching. With
106 targeted illumination, we are able to perform routine SomArchon voltage imaging from tens of
107 neurons over a large anatomical area of $360 \times 180 \ \mu m^2$, and over a prolonged recording duration
108 of several continuous minutes. These results demonstrate that targeted illumination with a DMD
109 represents a simple, low cost, and practical strategy for large scale voltage imaging of tens of
110 neurons over an extended period of time in awake behaving animals.

111

Results

Modeling and testing the effects of targeted illumination on optical crosstalk in widefield optical imaging

Motivated by the unique advantage of widefield microscopy in performing optical voltage imaging with high spatiotemporal resolution over large FOVs, we considered a targeted illumination approach to further enhance signal quality by reducing out-of-focus background signals. We first developed a theoretical model to estimate how targeted illumination minimizes signal crosstalk due to out-of-focus excitation or tissue scattering from nearby neurons that are not actively being imaged. We considered contributions from both out-of-focus fluorescence and tissue scattering, by modeling light propagation through scattering media using the radiative transfer equation in the forward scattering limit[24] (see Methods and Fig. S1). In our model, we characterized crosstalk values from non-targeted neurons at distance D_x laterally and D_z axially from a region of interest (ROI) under widefield versus targeted illumination conditions (Fig. 1a,b, Fig. S3). We found that in simulated fluorescence images, targeting illumination to a specific neuron substantially reduced the overall background in the imaging plane, and therefore reduced the strength of crosstalk from neighboring neurons (red circle: Fig. 1d,e). Additionally, the level of crosstalk contamination from a non-overlapping axially displaced neuron is strongly affected by the distance between the out-of-focus neurons relative to the imaging plane (Fig. 1c). These findings confirm that, for widefield microscopy, targeting illumination to a neuron of interest can improve signal quality by reducing the overall fluorescence background, and limiting signal contamination from neighboring out-of-focus neurons. These computational results highlight that targeted illumination is a viable approach for low-background, high-contrast imaging of voltage signals in the brain using widefield microscopy.

To experimentally evaluate the improvement of targeted illumination, we integrated a DMD into a custom-built widefield microscope configured for dual color GFP and SomArchon imaging (Fig. 1h). We performed voltage imaging of SomArchon expressing neurons, in both cell cultures and in the visual cortex and the hippocampus of awake head fixed mice. Since SomArchon protein is fused to the GFP reporter, static GFP fluorescent images were first taken to identify SomArchon expressing neuronal soma. The GFP fluorescence images were then used to generate templates for targeting illumination to the identified SomArchon positive neurons. Consistent with what was observed in our computational models, we found that restricting illumination to the soma reduced the overall background fluorescence and accordingly enhanced the contrast of SomArchon fluorescence in individual cells (Fig. 1f,g).

147
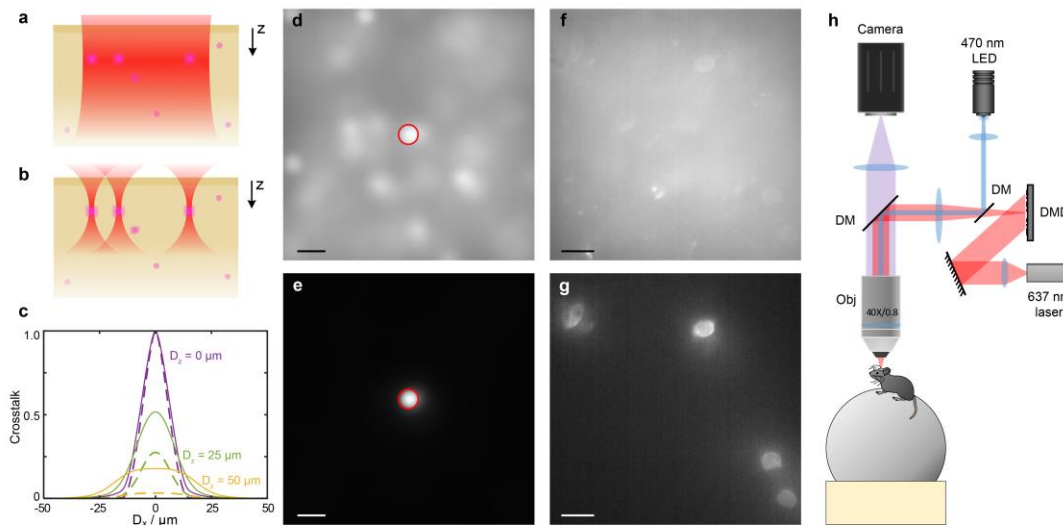
*Figure 1: Theoretic models of targeted illumination on fluorescence crosstalk in widefield optical imaging and a microscopy design for experimental testing in awake mice. (**a,b**) Illustration of the theoretical consideration of fluorescence imaging of individual neurons using widefield illumination (**a**) and targeted illumination (**b**). Purple dots illustrate the location of individual SomArchon expressing neurons. Red area illustrates the illumination beam for SomArchon excitation. (**c**) Characterization of fluorescence crosstalk values from a non-targeted neuron at a lateral distance D_x and axial distance D_z away from the neuron of interest under widefield and targeted illumination conditions. Solid lines, widefield illumination; dashed line, targeted illumination. Purple, D_z = 0 µm; green, D_z = 25 µm; yellow, D_z = 50 µm. (**d,e**) Simulated images of fluorescence from a single neuron under widefield illumination (**d**) and targeted (**e**) illumination. Illumination target is indicated by the red circle. (**f,g**) An example widefield versus targeted illumination voltage imaging experiment in an awake head fixed mouse positioned on a spherical treadmill shown in (**h**). SomArchon fluorescence of visual cortex neurons imaged with widefield illumination (**f**), and targeted illumination (**g**) of 4 individual neurons under the same laser power density. (**h**) Experimental setup. DM, dichromatic mirror; Obj, objective lens. Scale bars are 20 µm.*

163

Targeted illumination increases spike spike-to-baseline (SBR) ratio and reduces SomArchon photobleaching in cultured neurons

We first examined whether targeted illumination improves SomArchon voltage imaging quality in cultured neurons transduced with AAV9-syn-SomArchon. Cultured neurons on flat glass coverslips have little out-of-focus fluorescence originating from the out of plane z-axis, and therefore should only exhibit small amount of signal contamination (Fig. S2). To directly compare the effects of targeted versus widefield illumination, we alternated 20-second long imaging trials between the two illumination conditions for the same FOV (n = 226 neurons recorded from 16 FOVs).

172

Cultured neurons exhibit spontaneous subthreshold membrane voltage fluctuations that occasionally produce action potentials. Since SomArchon can detect subthreshold voltage

175   dynamics[3], the actual photon shot noise is mixed with real biological subthreshold voltage
176   fluctuations. Therefore, it is difficult to quantify the actual noise level and therefore accurately
177   evaluate SomArchon signal qualities by calculating the absolute signal to noise ratio. We thus
178   calculated the spike-to-baseline ratio (SBR), defined as the amplitude of the spike divided by the
179   amplitude of the baseline fluctuations, as an estimated performance metric of SomArchon in
180   recording individual spikes. Since neurons in intact networks have heterogenous synaptic input
181   patterns and membrane biophysical properties, this spike SBR measure is an underestimation of
182   SomArchon performance, but it provides an intuitive measure of the optical voltage signal quality
183   when the subthreshold membrane potential cannot be precisely controlled.

184   With targeted illumination, we detected a spike SBR of 5.7 ± 2.0 (mean ± standard deviation, from
185   226 neurons in 16 FOVs), significantly greater than that observed from the same neurons under
186   the widefield illumination condition (4.9 ± 1.4, Fig. 2h). Since the spike identification algorithm
187   relies on a custom spike SBR threshold, we investigated whether the increase in spike SBRs
188   depends on the threshold used to identify spikes. We found that across several chosen SBR
189   threshold values, targeted illumination consistently resulted in greater spike SBRs than widefield
190   illumination (Fig. S4, Table S3). Furthermore, targeted illumination resulted in more detected
191   spikes than that detected from the same neurons measured in the widefield condition (Fig. 2i).

192

193   We next examined fluorescence decay, calculated as the percent reduction of fluorescence
194   intensity over time, an important parameter that limits the duration of fluorescence imaging in
195   general. We found that with targeted illumination, SomArchon showed a slight fluorescence
196   decay of 2.15 ± 2.66% (mean ± standard deviation, n = 226 neurons) over a 20 s period,
197   significantly smaller than that observed under widefield illumination (2.99 ± 1.04%, Fig. 2j).
198   Together, these results demonstrate that targeted illumination significantly improves SomArchon
199   performance in terms of spike SBR and fluorescence decay, even in cultured neurons where out-
200   of-focus background is minimal.

201

202
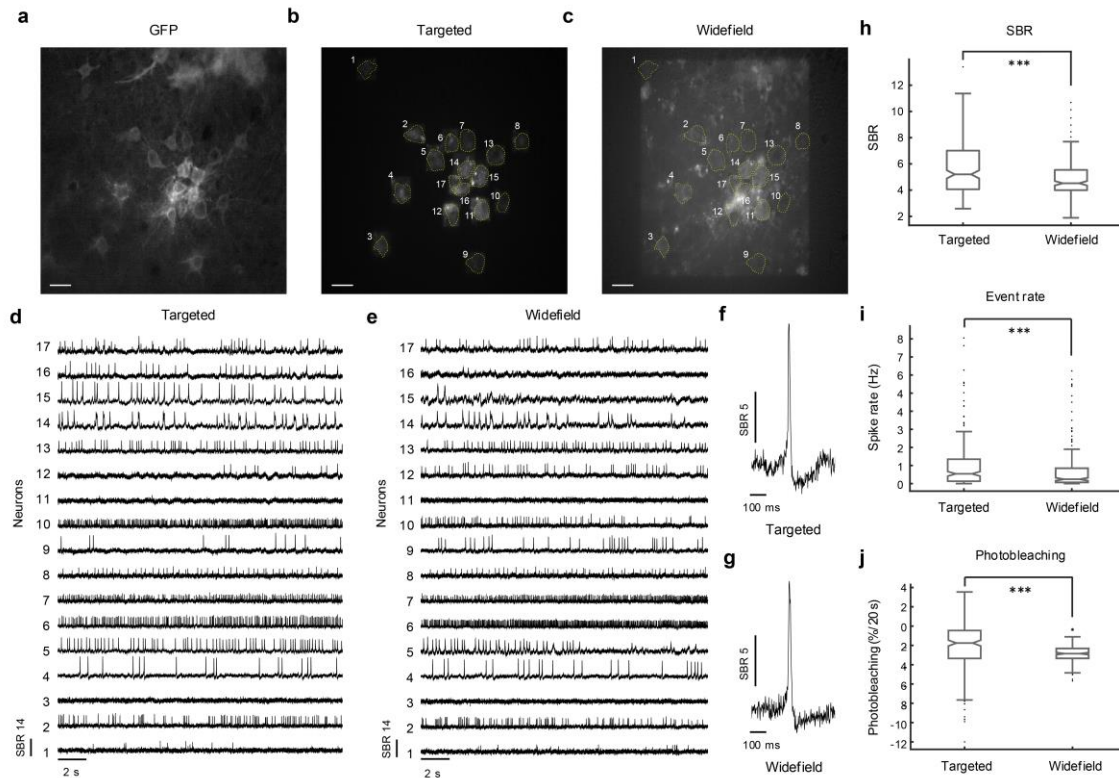
Figure 2. Targeted illumination increases spike SBR and reduces fluorescence decay in cultured neurons. (a-c) *An example FOV showing cultured neurons expressing SomArchon fused to a static GFP fluorophore; scale bars are 20 μm. (**a**) GFP fluorescence image under widefield illumination. (**b**) SomArchon fluorescence under targeted illumination. (**c**) SomArchon fluorescence under widefield illumination. (**d, e**) Example SomArchon fluorescence traces of 17 simultaneously recorded neurons in the FOV illustrated in A, using targeted illumination (**d**), and widefield illumination (**e**). (**f, g**) Example individual spikes recorded from the same neuron with targeted illumination (**f**) and with widefield illumination (**g**). (**h**) Spike SBR (***, p = 6.73e^{-14}, paired t-test comparing targeted illumination versus widefield illumination conditions, df = 204, n = 226 neurons from 16 FOVs). (**i**) Spike rate identified with a spike SBR threshold of 4.5 (***, p = 4.23e^{-5}, paired t-test, df = 225). (**j**) Reduction of SomArchon fluorescence over 20 seconds period (***, p = 9.06e^{-7}, paired t-test, df = 225). The illumination power density was ~2 W/mm² for both the target illumination and the widefield illumination conditions, for all recordings from cultured neurons. For all boxplots, the box indicates the median (middle line), 25th (Q1, bottom line), 75th (Q3, top line) percentiles, and the whiskers are Q1-1.5*(Q3-Q1), and Q3+1.5*(Q3-Q1). Outliers that exceed these values are shown as dots.*

219

Targeted illumination increases the cross-correlation of spikes, but minimally impacts cross-correlation of subthreshold membrane voltage in neuron cultures

With a high speed sCMOS camera, we were able to simultaneously image 2 - 28 neurons (14.13 ± 7.59, mean ± standard deviation, from 16 FOVs) at 500 Hz over a FOV of 360×180 μm². To estimate how targeted illumination can reduce signal crosstalk, we calculated the cross-correlation between neuron pairs, for both subthreshold voltage fluctuations (Vm) and spikes. We found that both Vm-Vm and spike-spike correlation decreased slightly with increasing
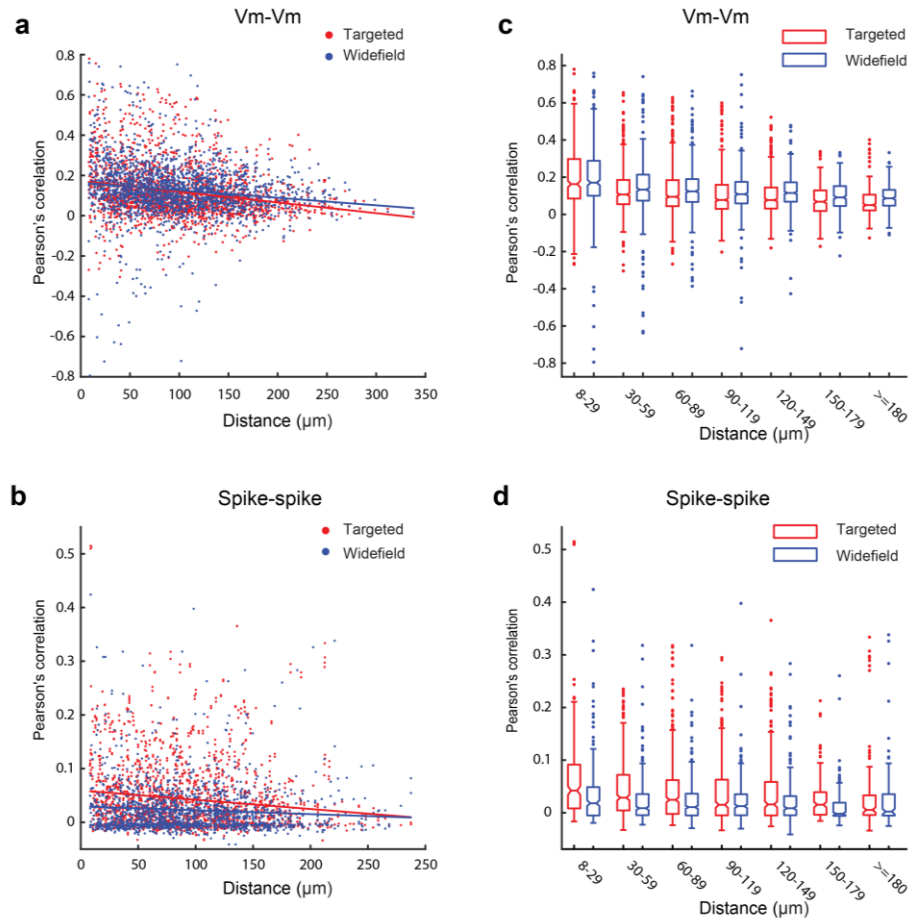
227   anatomical distance between simultaneously recorded neuron pairs (slopes for linear regression

228   between Vm-Vm correlation and distance are $-5.3e^{-4}$ and $-3.7e^{-4}$ for targeted illumination and

229   widefield illumination respectively, and between spike-spike correlation and distance are $-1.7e^{-4}$

230   and $-7.2e^{-5}$ respectively, Fig. 3a,b). The regression slopes of Vm-Vm correlation and spike-spike

231   correlation over anatomical distance under targeted illumination condition are both greater than

232   that observed during widefield illumination condition (Vm-Vm correlation, p = $5.3592e^{-6}$, z score

233   = -4.5502, permutation test; spike-spike correlation, p = 0.0039, z score = -2.8865).

234

235   To further evaluate changes in Vm-Vm and spike-spike correlation between the two illumination

236   conditions across different anatomical distances, we binned the correlation values of neuron pairs

237   every 30 μm. Consistent with the improvement of spike SBR observed under the targeted

238   illumination condition, spike-spike correlation was slightly greater under targeted illumination

239   than widefield illumination condition across neuron pairs within 180 μm, although no difference

240   was observed for neuron pairs over 180 μm (Fig. 3d). When we examined Vm-Vm correlation, we

241   found no difference between targeted illumination and widefield illumination conditions for

242   neurons pairs within 120 μm, though a slightly smaller correlation value was obtained under

243   targeted illumination for neurons over 120 μm away (Fig. 3c). The similar Vm-Vm correlations

244   under widefield and targeted illumination is consistent with our numerical models when the

245   sample is only a monolayer of cells absent of significant contributions from axial tissue scattering

246   (Fig. S2).

247

Figure 3. Targeted illumination effects on Vm-Vm correlation and spike-spike correlation in cultured neurons. (a,b) *Pearson's correlation between pairs of simultaneously recorded neurons decreased over anatomical distance for Vm-Vm correlation (**a**) and spike-spike correlation (**b**). Red dots indicate correlation values from pairs of neurons recorded under the targeted illumination condition. Blue dots indicate correlation values from pairs of neurons recorded under the widefield illumination condition. (**c,d**) Vm-Vm correlation (**c**) and spike-spike correlation (**d**) at different distances with 30 μm increment. Red boxplots are correlation values obtained with the targeted illumination condition, and blue boxplots are with the widefield illumination condition. For all boxplots, the box indicates the median (middle line), 25th (Q1, bottom line), 75th (Q3, top line) percentiles, and the whiskers are Q1-1.5*(Q3-Q1), and Q3+1.5*(Q3-Q1). Outliers that exceed these values are shown as dots. Refer to Tables S1 and S2 for statistical tests.*

<u>*Targeted illumination improves SomArchon spike SBR, reduces fluorescence crosstalk, and enables long-duration recording in the visual cortex of awake mice*</u>

To quantify the effect of targeted illumination in the brains of awake animals, we examined SomArchon expressing neurons in the superficial layers of visual cortex. Mice were head-fixed and free of voluntary locomotion on a spherical treadmill. For each FOV, we alternated 10-second long voltage imaging sessions between targeted illumination and widefield illumination conditions. We

267 found that targeted illumination significantly reduced SomArchon fluorescence decayed to 11.02
268 ± 3.08% over 10 seconds, approximate half of that observed with widefield illumination (20.38 ±
269 3.05%, p = 4.74^{-14}, paired t-test, df = 20, Fig. 4k). Targeted illumination also resulted in a significant
270 increase in SomArchon spike SBR, achieving 4.6 ± 0.7, significantly higher than the 4.1 ± 0.44
271 obtained with widefield illumination (p = 0.023, paired t-test, df = 18 neurons, Fig. 4l), similar to
272 that observed in cultured neurons (Fig. 2h). This significant increase in spike SBR for the targeted
273 illumination condition accordingly led to a greater number of spikes identified when spike SBR
274 threshold is used for spike identification (Fig. 4m).
275

276 To examine how targeted illumination impacts correlation measurements between
277 simultaneously recorded neuron pairs, we computed spike-spike and Vm-Vm correlations as
278 detailed above in cultured neuron experiments. Unlike in cultured neurons, here due to tissue
279 scattering and fluorescence from out-of-focus neurons, we observed that targeted illumination
280 significantly reduced Vm-Vm correlation values (Fig. 4n). However, spike-spike correlation values
281 remained largely similar under both conditions (Fig. 4o). Since spikes are only produced when Vm
282 depolarization reaches sodium channel activation threshold for action potential generation, joint
283 synaptic inputs that produce correlative low amplitude Vm changes between neuron pairs that
284 are subthreshold will not be captured by spike-spike correlation measures. The fact that Vm-Vm
285 correlation is reduced by targeted illumination highlights that Vm signals contain a higher
286 proportion of background signal crosstalk than spiking signals.
287
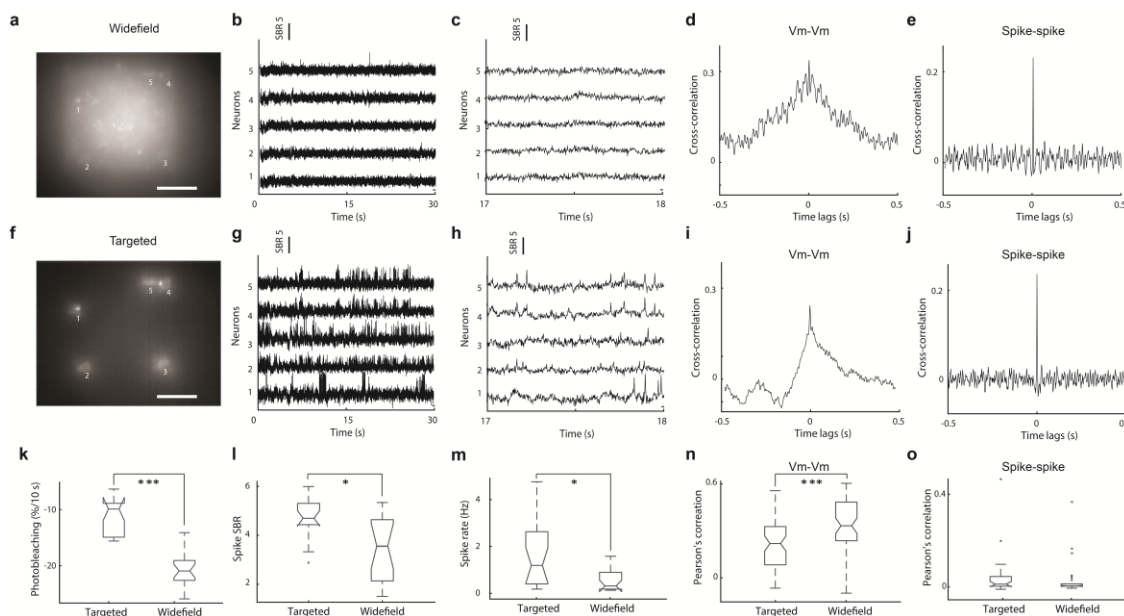
289 *Figure 4: Targeted illumination improves SomArchon voltage imaging performance. (a-e)*
290 *SomArchon fluorescence voltage imaging under widefield illumination condition. (a) An example*
291 *FOV showing SomArchon fluorescence intensity averaged over the recording session. Scale bar: 50*
292 *μm. (b,c) Example SomArchon fluorescence traces (b), and zoomed in view (c), from simultaneously*
293 *recorded 5 neurons indicated in (a) over a 10 s long recording period. (d,e) Example Vm-Vm (d)*
294 *and spike-spike correlation. (e) Cross-correlogram of a single neuron pair, neurons labeled 2 and*
295 *3 in (a). (f-j) SomArchon fluorescence voltage imaging under targeted illumination condition. (g-j)*
296 *Same plots and calculation as in (b-e), but for targeted illumination condition. (k) Fluorescence*

297 *decay over 10 seconds for widefield vs targeted illumination conditions (***, p = 4.74e^{14}, paired t-*
298 *test, df = 20). (l) Spike SBR for widefield vs targeted illumination conditions (*, p = 0.023, paired t-*
299 *test, df = 18). (m) Detected spike rates (*, p = 0.016, paired t-test, df = 18). (n) Vm-Vm correlations*
300 *between simultaneously recorded neuron pairs with targeted illumination versus widefield*
301 *illumination (***, p = 0.00027, paired t-test, df = 30). (o) Spike-spike correlation between*
302 *simultaneously recorded neuron pairs with targeted illumination versus widefield illumination (p*
303 *= 0.58, paired t-test, df = 30). The illumination power density was ~3 W/mm^2 for both the target*
304 *illumination and the widefield illumination conditions, for this and all other visual cortex*
305 *recordings. For all boxplots, the box indicates the median (middle line), 25th (Q1, bottom line),*
306 *75th (Q3, top line) percentiles, and the whiskers are Q1-1.5*(Q3-Q1), and Q3+1.5*(Q3-Q1).*
307 *Outliers that exceed these values are shown as dots.*

308

309 With targeted illumination, the drastically reduced background fluorescence and consequently
310 enhanced spike SBR allowed us to reduce illumination intensity during voltage imaging. This
311 reduction of overall ballistic illumination intensity, and the minimization of ROI exposure to
312 backscattered light, can help reduce SomArchon photobleaching and thus allowed for recording
313 over an extended duration under targeted illumination. In one example, we continuously
314 recorded from the same neurons over 5 minutes, and detected excellent spike SBRs throughout
315 the entire recording duration (Fig. 5). Of the two simultaneously recorded neurons, the spike SBR
316 for neuron 1 was 4.13 ± 1.1 (mean ± standard deviation, n = 1366 spikes), and for neuron 2 was
317 4.81 ± 1.29 (mean ± standard deviation, n = 261 spikes). However, we did notice a reduction in
318 spike SBR over time (p = 9e^{-14}, Kruskal-wallis, df = 1626 spikes, from 2 neurons combined), which
319 reflects the effect of fluorescence photobleaching.

320
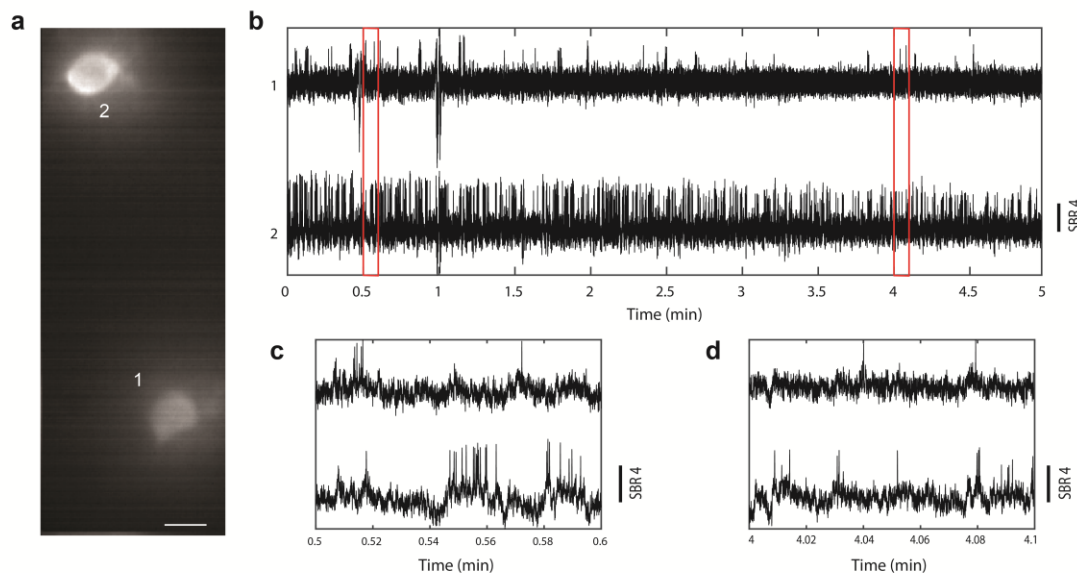
321

322 ***Figure 5: An example 5-minute long continuous recording session from two visual cortex***
323 ***neurons.*** *(a) SomArchon fluorescence image from two neurons visualized with targeted*
324 *illumination. Scale bar, 10 μm. (b) SomArchon fluorescence traces throughout the entire 5-minute*

long recording session. (c,d) Zoom-in view of SomArchon fluorescence towards the beginning (c) and the end of the recording session (d).

Targeted illumination allows for large scale recordings in CA1 of awake mice

Having established the significant advantage of targeted illumination, we deployed targeted illumination to image multiple neurons in the dorsal hippocampus CA1 region. Combining targeted illumination with a high-speed large sensor sCMOS camera, we can simultaneously image tens of neurons with a FOV of 360 × 180 μm^2. We performed 6 recordings of 17 or more CA1 neurons (37 ± 22 neurons per session, mean ± standard deviation), while mice were awake and head-fixed navigating the spherical treadmill. Across these recording sessions, we recorded a total of 222 spiking neurons, with a spike SBR of 4.16 ± 0.5 (mean ± standard deviation, n = 222 spiking neurons, Fig. 6, Fig. S5). In one recording, we were able to record 76 neurons simultaneously, and detected spikes in 58 of those neurons, over a 90-second long recording period (Fig. 6). The mean spike SBR of these neurons was 3.94 ± 0.4 (mean ± standard deviation, n = 58 neurons).
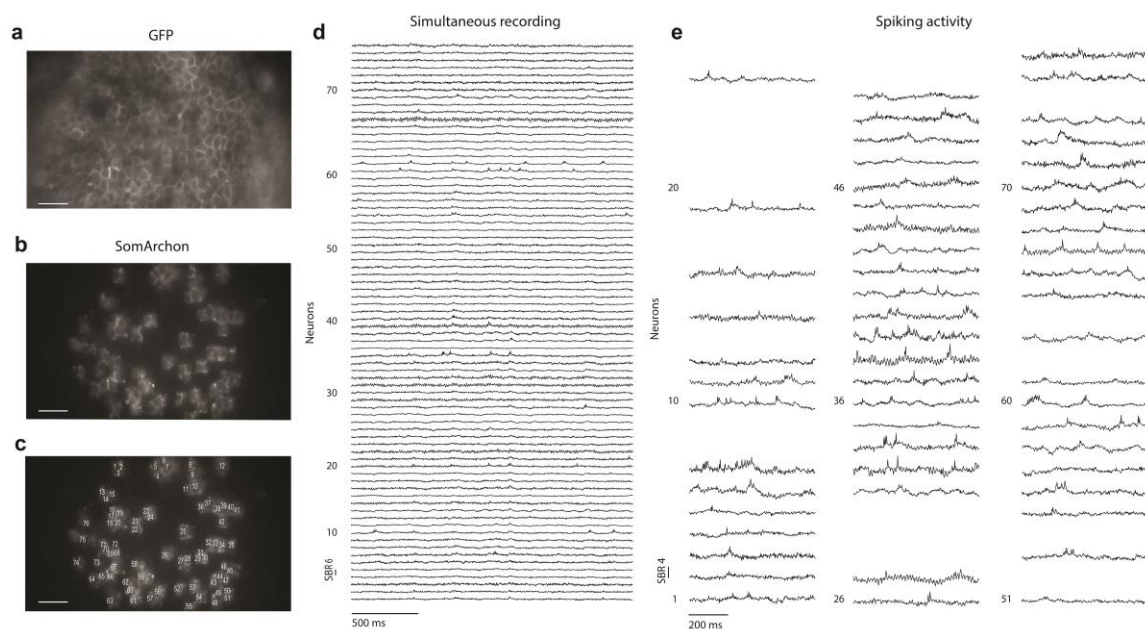
Figure 6: An example of 90-second long continuous recording from 76 CA1 neurons simultaneously using targeted illumination in a behaving mouse. (a-c) SomArchon expressing CA1 neurons in the FOV, visualized via GFP fluorescence (a), SomArchon fluorescence visualized with targeted illumination (b), and with each neuron labelled (c). Scale bar, 50 μm. (d) Example traces of simultaneously recorded 76 CA1 neurons. 2.5 seconds recordings are shown here. (e) Representative example spikes in the 58 neurons where spikes were detected. The illumination power density was 4-5W/mm^2 for this and all other CA1 recordings.

350   Further quantification of Vm-Vm and spike-spike correlation over anatomical distance between
351   simultaneously recorded CA1 neuron pairs revealed that both Vm-Vm and spike-spike
352   correlations substantially decreased with anatomical distance (Fig. 7, *Kruskal-wallis, p = 5.16e^{-7},*
353   *df = 5109 for Vm-Vm correlations; p = 3.18e^{-6}, df = 4771 for spike-spike correlations*). These results
354   are consistent with that observed in cultured neurons and reflect the general understanding that
355   nearby neurons tend to receive more temporally aligned synaptic inputs relative to neurons
356   further apart[25].

357
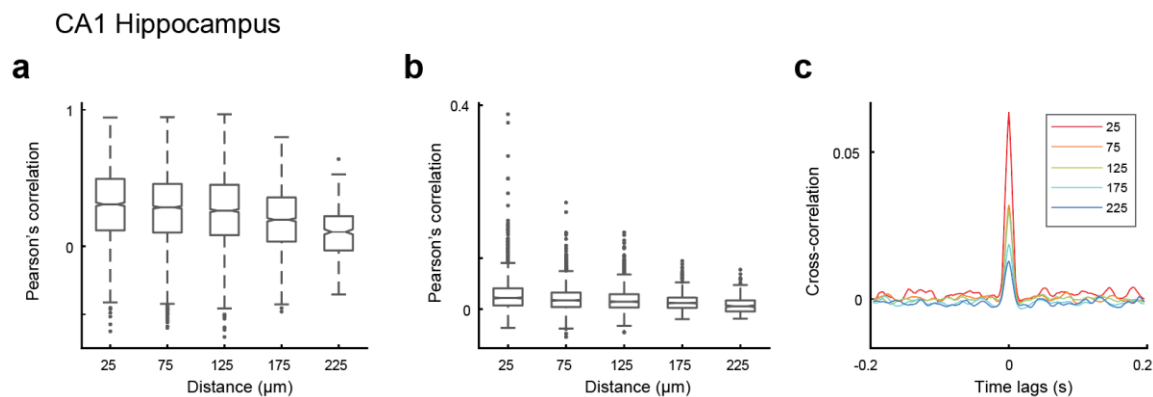
358

359   ***Figure 7:*** *Pearson's correlation values of spike-spike and Vm-Vm correlation over anatomical*
360   *distance. **(a)** Vm-Vm correlation of CA1 neuron pairs over distance. Correlation values are grouped*
361   *by distance (0 - 50 µm, 51 - 100 µm, 101- 150 µm, 151 - 200 µm, 201 - 250 µm). **(b)** Spike-spike*
362   *correlation of CA1 neurons over distance. **(c)** Average spike-spike cross-correlogram across all*
363   *recorded neuron pairs. For all boxplots, the box indicates the median (middle line), 25th (Q1,*
364   *bottom line), 75th (Q3, top line) percentiles, and the whiskers are Q1-1.5*(Q3-Q1), and*
365   *Q3+1.5*(Q3-Q1). Outliers that exceed these values are shown as dots.*

366

367   **Discussion**

368   Widefield microscopy remains an essential imaging technique for high-speed voltage imaging,
369   especially in task performing animals where a large FOV with high spatial resolution is required to
370   resolve the activity from many individual neurons simultaneously. To improve epi-fluorescence
371   microscopy for high speed, large scale, and long duration voltage imaging, we developed a simple,
372   low cost, DMD-based targeted illumination system that can be easily integrated into a custom
373   widefield microscope. We estimated the impact of background fluorescence on voltage imaging
374   theoretically, and then experimentally quantified the improvement of targeted illumination for
375   SomArchon voltage imaging performance in 2D neuron cultures and in the brains of behaving
376   mice. We found that by restricting illumination to neuronal cell bodies, we were able to
377   significantly increase SomArchon signal quality in terms of spike SBR and reduce out-of-focus
378   background fluorescence. These improvements were more substantial for *in vivo* brain imaging
379   than in cultured neurons, and were consistently observed across the two brain regions tested that
380   have varying labeling density, including the visual cortex with sparsely-labeled neurons and the
381   hippocampus with densely labeled neurons. With such improvements in SomArchon signal
382   quality, together with a high-speed large sensor size sCOMS camera, we were able to record

383 optical voltage signals from over 70 neurons simultaneously over a wide FOV of 360 × 180 μm^2 at
384 500 Hz.

385

386 One advantage of using targeted illumination is the reduced power density of excitation light,
387 from both direct ballistic excitation photons and backscattered photons from tissue scattering. In
388 this study, the ballistic excitation power density used for *in vivo* recordings was measured at 3 –
389 5 W/mm^2, which equals to 0.7 – 1.1 mW per neuron (assuming a 15 x 15 μm^2 square excitation
390 region). However, for *in vivo* imaging, the actual excitation power will be further affected by tissue
391 scattering. Photons targeting a cell can be scattered away from the ROI, whereas photons
392 targeting non-ROI regions could eventually reach an ROI due to forward and backward scattering.
393 Therefore, although the same excitation power density was applied to both targeted illumination
394 and widefield illumination conditions, neurons under widefield illumination conditions were
395 actually exposed to higher excitation, causing the greater observed fluorescence decay, due to
396 enhanced photobleaching of SomArchon. In addition, the improved spike SBR also allowed us to
397 reduce ballistic excitation power for targeted illumination. As a result, we were able to perform
398 continuous recordings over many minutes in duration, with only moderate reductions in spike
399 SBR. While the performance of fluorescence based activity indicators are always limited by
400 photobleaching, deploying trial-based study designs without excitation illumination during inter-
401 trial-intervals should allow SomArchon to measure membrane voltage over many trials, and
402 potentially over a greater cumulative period of time than demonstrated here using continuous
403 illumination.

404

405 To estimate SomArchon fluorescence quality, we calculated spike to baseline ratio (SBR). The
406 baseline used in this SBR calculation contains both biological subthreshold membrane voltage
407 fluctuations and SomArchon intrinsic fluorescent shot noise. While artificially setting neuronal
408 voltage below action potential threshold, as often practiced in voltage clamp experiments, helps
409 minimize the impact of synaptic potentials during non-spiking period to allow for estimation of
410 the fluorescence sensor shot noise, it is not meaningful in the context of *in vivo* experiments.
411 Neurons in intact neural circuits, especially in the awake brain, receive heterogenous synaptic
412 inputs and exhibit distinct membrane biophysical properties, which lead to variation in
413 subthreshold membrane voltage fluctuations that are difficult to estimate. Thus, spike SBR
414 estimation for each neuron cannot fully capture the quality of SomArchon signal contrasts, and
415 represents an underestimation of SomArchon performance. However, spike SBRs of the same
416 neuron when compared under the two illumination conditions can provide a quantitative
417 measure of the fluorescence signal quality, providing direct experimental evidence that targeted
418 illumination significantly improve fluorescence quality of SomArchon voltage imaging. Since spike
419 SBR is a key consideration for spike detection, the fact that we detected more spikes under
420 targeted illumination condition further demonstrates the improvement of SomArchon voltage
421 signal quality.

422

423 Compared to other systems, such as the spatial light modulator-based holographic targeting
424 technique[6], which provides similar benefit of reduced background and enhanced SBR, our DMD-

425   based targeted illumination system is more cost-effective, much simpler to implement, and covers
426   a much larger FOV. Although two-photon microscopy offers inherent background rejection[26], the
427   requirement for high acquisition speed has not made it conducive to voltage imaging with a few
428   notable exceptions[4,19,27,28], all of which involve significant technical challenges in terms of the
429   optical setup. More importantly, these demonstrations have also been limited to simultaneous
430   imaging of a few neurons for several seconds in duration.

431

432   A further consideration is that imaging living animals will always be subject to fine movement due
433   to metabolic, physiologic, and vascular changes, which can be corrected via image registration[29,30].
434   Targeting illumination only to cell membranes using holographic projections is sensitive to
435   translational movement due to restricted area of illumination, which may make it difficult to
436   deploy during behavior in animals. In contrast, DMD-based targeting has the flexibility to adjust
437   the illumination window size to accommodate fine biological motion during awake and behaving
438   conditions. For example, increasing the region of targeted illumination to capture the
439   morphological details of a neuron allows for fine translational movement that can be effectively
440   corrected after image acquisition. Single photon widefield imaging is also more amenable to axial
441   motions due to the lack of optical sectioning[20], which allows for continuous recording of signal
442   during subtle fluctuations in axial positions. While such advantage is retained to some degree over
443   the illuminated regions with DMD-based targeted illumination, it is less so when using holographic
444   projections. Techniques with confined excitation volume limited to narrow z-axis profiles, such as
445   two-photon microscopy[26], are much more sensitive to image motion expected from behaving
446   animals[31].

447

448   Combining DMD-based targeted illumination with the fully genetically encoded SomArchon and
449   a high-speed large area sCMOS camera, we were able to record dozens of neurons concurrently,
450   over extended periods of time. The capability of sampling both subthreshold voltage fluctuations
451   and action potentials from a large number of neurons will enable new experimental designs that
452   are otherwise not feasible with lower throughput intracellular voltage measurement techniques,
453   such as patch-clamp or sharp electrode recording approaches. With continued improvement of
454   GEVIs, simple optical voltage imaging instrumentation as presented here can be easily adopted
455   across a broad number of neuroscience studies.

456

457   **Acknowledgements**

458

459   **Author Contributions**

460   S.X., E.L., H.J.G, and J.S. performed all experiments. S.X. produced the simulated data model.
461   E.L., P.F., and Y.W. analyzed the data. R.M. provided surgical expertise and H.T. consulted on
462   imaging data analysis. H.M. provided *in vitro* resources and J.M. consulted on imaging system

463   design. X.H. supervised the study. S.X, E.L., H.J.G, and X.H. wrote the manuscript. All authors
464   edited the manuscript.

465

Declaration of Interests
466

467   The authors declare no competing interests.

468

Financial Disclosure
469

476

477 **Methods**

478 **Simulated data theory for widefield fluorescence imaging**

479 We consider the problem of widefield fluorescent imaging in a mouse brain in the context of
480 imaging through scattering media within the forward scattering limit. In our model (Fig. S1), an
481 incoherent source located at plane $z = 0$ is embedded at depth $z = z_t$ inside a scattering
482 medium, whose scattering properties are characterized by the scattering phase function $p(\hat{\mathbf{s}})$,
483 mean scattering length l_s, and anisotropic factor $g \approx 1$. The image of the scattered light field
484 from the source is relayed by a unit magnification $4f$ system and recorded by a detector that's
485 conjugate to the plane $z = z_s$ in the sample space. Within the scattering medium, light
486 propagation can be characterized in terms of radiance $\mathcal{R}(z, \boldsymbol{\rho}, \hat{\mathbf{s}})$ using a simplified radiative
487 transport equation by invoking small angle approximation[24]:

$$\frac{\partial}{\partial z}\mathcal{R}(z, \boldsymbol{\rho}, \hat{\mathbf{s}}) + \hat{\mathbf{s}} \cdot \nabla\mathcal{R}(z, \boldsymbol{\rho}, \hat{\mathbf{s}}) = -\frac{1}{l_s}\mathcal{R}(z, \boldsymbol{\rho}, \hat{\mathbf{s}}) + \frac{1}{4\pi l_s}\int p(\hat{\mathbf{s}} - \hat{\mathbf{s}}')\mathcal{R}(z, \boldsymbol{\rho}, \hat{\mathbf{s}}')d^2\hat{\mathbf{s}}' \quad (1)$$

488 where $(\boldsymbol{\rho}, z) = (x, y, z)$ is the 3D position vector, $\hat{\mathbf{s}} = (\theta_x, \theta_y, 0)$ is a unit direction vector
489 parameterized by the two angles assumed to be small, where $\theta_{x,y} \approx 0$.

490 To solve Eq. (1), it is necessary to establish a boundary condition, which, in our case, can be
491 expressed as an isotropic emitter with intensity distribution $I_0(\boldsymbol{\rho}_0)$ located at axial position $z_0 =$
492 0

$$J_0(\boldsymbol{\rho}_c, \boldsymbol{\rho}_d, z_0) = \frac{1}{\kappa^2}I_0(\boldsymbol{\rho}_c)\delta(\boldsymbol{\rho}_d) \quad (2)$$

493 where $\kappa = n/\lambda$, n is the refractive index, λ is the wavelength. Note that here we expressed the
494 boundary condition in terms of mutual coherence function $J(\boldsymbol{\rho}_c, \boldsymbol{\rho}_d, z) = \langle E(\boldsymbol{\rho}_+, z)E^*(\boldsymbol{\rho}_-, z)\rangle$,
495 where $\boldsymbol{\rho}_\pm = \boldsymbol{\rho}_c \pm \boldsymbol{\rho}_d/2$, instead of radiance $\mathcal{R}(z, \boldsymbol{\rho}, \hat{\mathbf{s}})$. This is because for an imaging system, we
496 are more interested in the propagation of mutual coherence since it characterizes correlations of
497 light fields between pairs of points that contribute to the final fluorescence intensity. This
498 quantity, under paraxial limit, is related to the radiance of light field as

$$J(\boldsymbol{\rho}_c, \boldsymbol{\rho}_d, z) = \int \mathcal{R}(z, \boldsymbol{\rho}_c, \hat{\mathbf{s}})e^{i2\pi\kappa\hat{\mathbf{s}}\cdot\boldsymbol{\rho}_d}d^2\hat{\mathbf{s}} \quad (3)$$

499 Eq. (1) together with the boundary condition Eq. (2) can be solved analytically using double
500 Fourier transform[24]. We can therefore find the mutual coherence function at the surface of the
501 scattering medium $z = z_t$ as

$$J_0(\boldsymbol{\rho}_{0c}, \boldsymbol{\rho}_{0d}, z_t) = \frac{e^{-H(z_t, \boldsymbol{\rho}_{0d})}}{z_t^2}\int I_0(\boldsymbol{\rho}_0)e^{-i2\pi\frac{\kappa}{z_t}(\boldsymbol{\rho}_0 - \boldsymbol{\rho}_{0c})\cdot\boldsymbol{\rho}_{0d}}d^2\boldsymbol{\rho}_0 \quad (4)$$

502 where $H(z, \boldsymbol{\rho}) = \frac{1}{l_s}\int_0^z\left[1 - \frac{1}{4\pi}P(\kappa\boldsymbol{\rho}z'/z)\right]dz'$, and $P(\boldsymbol{q}) = \int p(\boldsymbol{s})e^{i2\pi\boldsymbol{s}\cdot\boldsymbol{q}}d\boldsymbol{s}$ is the Fourier
503 transform of the scattering phase function. This light field can be further propagated through a
504 $4f$ imaging system, resulting in the measured intensity at the detector plane as

$$I_d(\boldsymbol{\rho}_{1c}, z_s, z_t) = \iint \mathrm{CSF}\left(\boldsymbol{\rho}_{1c} - \boldsymbol{\rho}_{0c} - \frac{1}{2}\boldsymbol{\rho}_{0d}, z_s - z_t\right) \mathrm{CSF}^*\left(\boldsymbol{\rho}_{1c} - \boldsymbol{\rho}_{0c} + \frac{1}{2}\boldsymbol{\rho}_{0d}, z_s - z_t\right) J_0(\boldsymbol{\rho}_{0c}, \boldsymbol{\rho}_{0d}, z_t) d^2\boldsymbol{\rho}_{0c} d^2\boldsymbol{\rho}_{0d} \tag{5}$$

505 where $\mathrm{CSF}(\boldsymbol{\rho}, z) = e^{i2\pi\kappa z} \int \mathrm{CTF}(\boldsymbol{\kappa}_\perp) e^{i2\pi\boldsymbol{\rho}\cdot\boldsymbol{\kappa}_\perp - i\pi\frac{z}{\kappa}\kappa_\perp^2} d^2\boldsymbol{\kappa}_\perp$ is the 3D coherent spread function,

506 $\mathrm{CTF}(\boldsymbol{\kappa}_\perp) = A\left(\frac{f_0}{\kappa}\boldsymbol{\kappa}_\perp\right)$ is the in-focus coherent transfer function, $A(\boldsymbol{\xi})$ is the microscope aperture,

507 and f_0 is the focal length of the imaging lenses[18]. Note that here we assumed unit magnification

508 and refractive index of the medium $n = 1$.

509 From Eq. (4) and Eq. (5), using the definition of optical transfer function we therefore have the 3D
510 scattering optical transfer function (SOTF) for imaging a fluorescent object embedded in
511 scattering media as:

$$\mathrm{SOTF}(\boldsymbol{\kappa}_d, z_s, z_t) = \frac{e^{-H\left(z_t, \frac{\boldsymbol{\kappa}_d}{\kappa}z_t\right)}}{\kappa^2} \int \mathrm{CTF}\left(\boldsymbol{\kappa}_c + \frac{1}{2}\boldsymbol{\kappa}_d\right) \mathrm{CTF}^*\left(\boldsymbol{\kappa}_c - \frac{1}{2}\boldsymbol{\kappa}_d\right) e^{-i2\pi\frac{z_s}{\kappa}\boldsymbol{\kappa}_c\cdot\boldsymbol{\kappa}_d} d^2\boldsymbol{\kappa}_c \tag{6}$$

512 Eq. (6) is the main results that we use for simulating widefield neuronal imaging, the
513 interpretation of which is that the propagation of mutual coherence can be simply considered as

514 free space propagation with an additional attenuation factor $e^{-H\left(z_t, \frac{\boldsymbol{\kappa}_d}{\kappa}z_t\right)}$ due to scattering. Note
515 that this result not only holds for imaging of fluorescent signals in the detection path, but can also
516 be applied to delivering illumination patterns onto a scattering sample in the excitation path (i.e.,
517 targeted illumination).

518 Biological tissues such as the brain are typically characterized by strong forward scattering where
519 $g \approx 1$, where the distribution of scattering angles follows the Henyey-Greenstein phase
520 function[32]:

$$p(\hat{s} - \hat{s}') = p(\Delta s) = \frac{1 - g^2}{[(1 - g)^2 + g\Delta s^2]^{3/2}} \tag{7}$$

521 Assuming a circular microscope aperture of radius r, substituting Eq. (7) into Eq. (6) and using the
522 Stokseth approximation of free space 3D optical transfer function (OTF)[33], we arrive at the
523 analytical solution of the 3D SOTF:

$$\mathrm{SOTF}(\boldsymbol{\kappa}_\perp, z_s, z_t) = e^{-H\left(z_t, \frac{\boldsymbol{\kappa}_\perp}{\kappa}z_t\right)} \mathrm{OTF}(\boldsymbol{\kappa}_\perp) \mathrm{jinc}\left[\pi z_s \Delta\kappa_\perp \frac{\boldsymbol{\kappa}_\perp}{\kappa}\left(1 - \frac{\boldsymbol{\kappa}_\perp}{\Delta\kappa_\perp}\right)\right] \tag{8}$$

524 where $\Delta\kappa_\perp = 2NA/\lambda$, $NA = r/f_0$ is the numerical aperture of the system, and

$$\mathrm{OTF}(\boldsymbol{\kappa}_\perp) = \frac{2}{\pi}\left[\cos^{-1}\left(\frac{\boldsymbol{\kappa}_\perp}{\Delta\kappa_\perp}\right) - \frac{\boldsymbol{\kappa}_\perp}{\Delta\kappa_\perp}\sqrt{1 - \left(\frac{\boldsymbol{\kappa}_\perp}{\Delta\kappa_\perp}\right)^2}\right] \tag{9}$$

525 is the in-focus free space OTF. With Eq. (8), we can calculate the detected image or projected
526 pattern simply by filtering the original object/pattern in frequency space using the corresponding
527 SOTF.

528 **Simulation of widefield illumination versus targeted illumination conditions**

529   Using the theoretical model developed above, we compared the background fluorescence signals
530   generated using widefield and targeted illumination. We estimated the reduction of background
531   fluorescent signals from non-targeted SomArchon expressing neurons, or in other words, signal
532   cross-contamination, with the use of targeted illumination compared to standard widefield
533   illumination. For simplicity, here we only modeled a pair of neurons that are separated by a
534   distance D_x laterally and D_z axially (Fig. S2 and Fig. S3). Each neuron was assumed to be a 15 μm
535   diameter uniformly fluorescent sphere. For widefield illumination, the entire FOV was illuminated
536   equally. For targeted illumination, only a 15 μm circular ROI was projected onto the sample
537   centered at the location of the neuron of interest. Although both neurons were imaged onto the
538   camera, only the targeted one contained the signal, and the contribution from the other non-
539   targeted neuron within the ROI of the targeted neuron (the red circle in Fig. S2 d-i and Fig. S3 c-
540   h) was considered as background (or crosstalk).

541   In the simulation, we assumed the imaging system has unit magnification and $NA = 0.4$. The
542   excitation and emission wavelength are $\lambda_{ex} = 637 \text{ nm}$, $\lambda_{em} = 670 \text{ nm}$ respectively, with
543   corresponding tissue anisotropic factor $g_{637\text{nm}} = 0.89$, $g_{670\text{nm}} = 0.90$, and mean scattering
544   length $l_{s,637\text{nm}} = 110 \text{ μm}$, $l_{s,670\text{nm}} = 119 \text{ μm}$ [34]. Two different scenarios for optical voltage
545   imaging were considered, namely *in vitro* imaging in 2D neuronal cell culture and *in vivo* imaging
546   in a mouse brain.

547   For *in vitro* imaging in cultured neurons, since it typically consists of a monolayer of cells, we
548   therefore assumed the two neurons are at the same depth $z_t = 0$ (Fig. S2 a,b) with no tissue
549   scattering. By varying lateral distance D_x, we plotted the amount of crosstalk induced by the non-
550   targeted neurons in Fig. S2 c. Both widefield illumination and targeted illumination introduce
551   similar amount of crosstalk, as confirmed by our *in vitro* imaging experiments. Note that in reality,
552   these two neurons should not overlap in space and should have a separation at least $D_x = 15 \text{ μm}$
553   (although $D_x < 15 \text{ μm}$ is still plotted for completeness), in which case the amount of crosstalk is
554   close to 0. Therefore, we expect very little benefit of using targeted illumination for reducing
555   crosstalk in *in vitro* imaging. However, targeted illumination still pertains certain advantages over
556   widefield illumination in terms of photobleaching and SBR because of the reduction of stray light
557   and non-specific background signals.

558   For *in vivo* imaging in a mouse brain, we assumed that the targeted neuron was located at depth
559   $z_t = 100 \text{ μm}$ (see Fig. S3 a,b) inside the tissue with scattering properties given above. The amount
560   of crosstalk at positions with varying D_x and D_z are plotted in Fig. 1c. In this case, targeted
561   illumination results in much higher reductions in crosstalk, with most significant effects when out-
562   of-focus ($D_z \neq 0$). Example images of the non-targeted neuron at a defocus distance $D_z = 15 \text{ μm}$
563   with varying lateral displacement $D_x = 0 \text{ μm}, 10 \text{ μm}, 20 \text{ μm}$ are given in Fig. S3 c-h, where one
564   can see much lower intensity from the non-targeted neuron, with the crosstalk under targeted
565   illumination only at 76%, 44% and 3.8% of the values under widefield illumination.

566   Note that here our simulation only considers a pair of neurons, so the induced crosstalk values
567   are relatively low. For *in vivo* imaging where a much higher number of neurons are labeled, the
568   signal cross-contaminations can be introduced by tens or hundreds of neurons collectively. In this
569   case, the background with widefield illumination would be more detrimental as to render the in-

570 focus neuron visually indiscernible (see Fig. 1d-g), which could further necessitate the use of
571 targeted illumination.

572 **Cell cultures:**

573 Rat cortical neuron cultures were dissociated from E18 rat embryos (Charles River) and plated on
574 coverslips coated with poly-D lysine (Millipore Sigma cat # P2636) at 0.1 mg/mL in 0.1M borate
575 buffer (pH 8.5), and bathed with plating medium containing DMEM/F12 (Gibco cat. # 21331020)
576 supplemented with 10% Heat Inactivated FBS (R&D systems cat. # S11150), 5% Heat Inactivated
577 Horse Serum (Thermo Fisher Scientific cat. # 26050070), 1% Penicillin/Streptomycin (Thermo
578 Fisher Scientific cat. # 15140122), 397 µM L-Cysteine hydrochloride (Millipore Sigma cat. #
579 C1276), and 2 mM L-Glutamine (Thermo Fisher Scientific cat. # 35050061) (O'Connor 2020). 24
580 hours after plating, cells were switched to a feeding medium containing NBM (Gibco cat. #
581 21103049) supplemented with 1% Heat Inactivated Horse Serum (Thermo Fisher Scientific cat. #
582 26050070), 2% NeuroCult SM1 supplement (Stimcell Technologies cat. # 05711), and 1.4%
583 penicillin/streptomycin (Thermo Fisher Scientific cat. # 15140122) and 800 µM L-Glutamine. 11
584 days later, 5-fluoro-2-deoxyuridine (Millipore cat. # 343333) was added at a concentration of 4
585 µM to prevent glial cell overgrowth. 50% of the cell culture medium was exchanged every 3 days.
586 Neurons were transduced with 0.25 µL of AAV9-syn-SomArchon per well in 0.25 mL of feeding
587 media, 3-4 days after plating. Cells were imaged 14-16 days after plating, in an imaging buffer
588 containing 145 mM NaCl, 2.5 mM KCl, 10 mM glucose, 10 mM HEPES, 2 mM $CaCl_2$, and 1 mM
589 $MgCl_2$, pH 7.4.

590 **Animal surgical procedures**

591 All procedures involving animals were approved by the Boston University Institutional Animal
592 Care and Use Committee (IACUC). C57BL/6 adult female mice (3-6 months old on the day of
593 recording) were used in this study. Mice were surgically implanted with an imaging chamber and
594 a head-plate as described previously[3]. AAV-syn-SomArchon was injected either through an
595 infusion cannula attached to the window after the surgery, or injected during the surgery.

596 **Custom widefield optical imaging setup**

597 We customized a dual color epi-fluorescence fluorescence microscope, which used a 470 nm LED
598 (Thorlabs, M470L3) for GFP fluorescence excitation, and a 637 nm fiber-coupled laser (Ushio
599 America Inc., Necsel Red-HP-FC-63x) for SomArchon fluorescence excitation. The two illumination
600 channels were combined using a dichromatic mirror (Thorlabs, DMLP550R) and subsequently
601 directed onto the sample. The generated fluorescent signal was epi-collected by a microscope
602 objective (Nikon, 40×/0.8NA CFI APO NIR) and imaged onto a camera (Hamamatsu, ORCA-
603 Lightning C14120-20P) with a 175 mm tube lens. A combination of excitation filter, dichromatic
604 mirror, and emission filter (Semrock, LF405/488/532/635-A-000) was used to separate
605 fluorescent signals from the excitation light.

606 To pattern the illumination in the SomArchon imaging channel, the output of the 637 nm
607 multimode laser was collimated (Thorlabs, F950SMA-A), expanded (Thorlabs, BE02M-A), and
608 directed onto a DMD (Vialux, V-7000 VIS) at approximately 24° to its surface normal. The DMD
609 was further imaged onto the sample with a 175 mm lens and the objective, so that only sample
610 regions corresponding to the 'on' pixels of DMD were illuminated. The axial position of the DMD
611 was adjusted so that it is conjugate to the camera, and an additional affine transform was

612 estimated to register the pixels between the DMD and the camera. The DMD was controlled using
613 custom Matlab script based on Vialux ALP-4.2 API.

614 During each imaging session, a GFP fluorescence image was first taken for illumination target
615 identification, where a small rectangular ROI was manually selected for each individual neuron to
616 be imaged. A binary illumination mask was then generated based on all the selected ROIs and
617 uploaded to the DMD for illumination targeting. SomArchon voltage imaging was performed at
618 500 Hz, with 2 × 2 pixel binning, resulting in an imaging area of 1152 × 576 pixels on the sCMOS
619 camera sensor, corresponding to a 360 × 180 μm^2 FOV at the sample. To estimate sCMOS camera
620 dark level and intrinsic noise, videos were collected with the camera set to the same acquisition
621 parameters as during regular imaging experiments, but without light exposure (500 Hz, 2 × 2 pixel
622 binning, 1152 × 576 pixels imaging area). The sensor dark level was estimated to be 767.7, with
623 an intrinsic noise of 12.6 (standard deviation) per pixel.

624 **Data analysis**

625 All imaging data were acquired by HCImage software (Hamamatsu), and further processed using
626 MATLAB (Mathworks) offline.

627 **Neuron ROI selection**

628 All data analysis was performed offline in Matlab 2019b or 2020a. SomArchon fluorescence
629 images were first motion corrected using a pairwise rigid motion correction algorithm as
630 described previously[29]. For targeted illumination recordings, each ROI was centered on a neuron
631 of interest, with the ROI size slightly greater than the outline of the neurons, so that motion
632 correction can be performed on each targeted ROI that had distinguishable features identifiable
633 by the algorithm. After motion correction, we manually selected ROIs corresponding to individual
634 neurons, based on the average SomArchon fluorescence image during the first recorded trial. ROIs
635 were cross-referenced by comparing SomArchon fluorescence with the stable EGFP fluorescence.
636 The identified neurons were then applied to all subsequent trials in the same recording session.
637 SomArchon fluorescence traces were then extracted for each neuron by averaging all the pixels
638 within the neuron across the entire experiments. For direct comparison of SomArchon
639 fluorescence of the same neurons between widefield and target illumination conditions, the same
640 neuron ROIs were used for both recording conditions. Trace time segments with sharp, drastic
641 changes in fluorescence (e.g. due to motion) were detected as outliers and excluded from further
642 analysis in both the widefield and targeted illumination analysis. Specifically, for the outlier
643 detection we applied the generalized extreme Studentized deviate test on the moving standard
644 deviation values using a sliding window of ±60 ms on spike-removed traces (see Method Section
645 spike detection and spike SBR calculation). In some cases, not all time points during the period of
646 an artefact were marked as outliers. Time points between outliers (< 3 data points) were therefore
647 interpolated. To remove further artefacts, we excluded time points that were 6 standard
648 deviations outside the trace fluorescence distribution. Time points between and around the
649 detected outliers were also removed (±350 ms) as those periods often coincided with extended
650 animal motion artefacts.

651 **Fluorescence decay estimation**

652   To estimate SomArchon fluorescence decay, we first removed spikes by applying a median filter
653   (window of 51 frames), and then subtracted the camera dark level (measured as 767.7). We
654   calculated fluorescence decay as the ratio of the mean fluorescence intensity during the first 600
655   ms and that during the last 600 ms for each trial, and then averaged across all trials. In cultured
656   neurons, we detected a drastic fluorescence drop within the first couple seconds of recording,
657   likely mainly due to bleaching of autofluorescence unrelated to SomArchon, thus we excluded the
658   first trial from subsequent analysis for culture neuron analysis.

659   **Spike detection and spike SBR calculation**

660   To separate spikes from subthreshold voltage fluctuations, we first generated a "Smoothed Trace"
661   (ST) by averaging the fluorescence trace using a moving window of ±100 frames. To estimate
662   baseline fluctuation, we first removed potential spikes by replacing any fluorescence values above
663   ST with the corresponding values of ST. The amplitude of the baseline fluctuation was then
664   estimated as 2 times the standard deviation of the resulting trace, since half of the fluctuations
665   were removed in the spike removal step described above. For spike SBR estimation, we also
666   subtracted the camera intrinsic noise (standard deviation = 12.6 per pixel) from the trace noise to
667   obtain camera-independent estimates.

668   For spike detection, we first removed small subthreshold rapid signal changes by replacing the
669   fluorescence below ST with corresponding values of ST. The derivative of the resulting trace was
670   then used for spike detection, where spikes were identified as the time points above 4.5 times of
671   the standard deviation of the resulting derivative trace. Spike amplitude was calculated as the
672   peak fluorescence for each spike minus the mean of the fluorescence during the three time points
673   before spike onset. Spike SBR was calculated as spike amplitude divided by the amplitude of
674   baseline fluctuations described above.

675   **Pearson correlation analysis**

676   Pearson cross-correlation was performed using the Matlab functions *corrcoef* and *xcorr,* for both
677   Vm-Vm and spike-spike correlation analysis. To calculate spike-spike correlation, spike vectors
678   were smoothed over a ±10 ms time window for each spike before applying correlation analysis.
679   To calculate Vm-Vm correlation, we removed spikes by replacing 3 data point centered at each
680   identified spike times with the adjacent values that largely eliminated the contribution of spikes
681   in Vm-Vm correlation analysis.

682   **Statistical analysis**

683   Paired student's t-tests were used for comparisons involving the same neurons between the
684   targeted illumination condition and the widefield illumination condition. A Kolmogorov-Smirnov
685   test was used to test the difference of cross-correlation over distance between targeted
686   illumination and widefield illumination conditions. For Kolmogorov-Smirnov test, the data in
687   each of the two conditions were first sorted by distance before comparing. A Friedman's test, 2
688   factor non-parametric ANOVA, was used to compare the difference between the average
689   correlations of each bin in Fig. 3.

690   **Data and software availability statement**

691   Codes used for data analysis is available on our lab website and Github repository:

692   https://www.bu.edu/hanlab/resources/ and https://github.com/HanLabBU

693

694 **References**

695 1. Gong, Y. *et al.* High-speed recording of neural spikes in awake mice and flies with a
696   fluorescent voltage sensor. *Science* **350**, (2015).

697 2. Abdelfattah, A. S. *et al.* Bright and photostable chemigenetic indicators for extended in
698   vivo voltage imaging. *Science* **365**, (2019).

699 3. Piatkevich, K. D. *et al.* Population imaging of neural activity in awake behaving mice.
700   *Nature* **574**, (2019).

701 4. Villette, V. *et al.* Ultrafast two-photon imaging of a high-gain voltage indicator in awake
702   behaving mice. *Cell* **179**, (2019).

703 5. Adam, Y. *et al.* Voltage imaging and optogenetics reveal behaviour-dependent changes in
704   hippocampal dynamics. *Nature* **569**, (2019).

705 6. Fan, L. Z. *et al.* All-optical electrophysiology reveals the role of lateral inhibition in sensory
706   processing in cortical layer 1. *Cell* **180**, (2020).

707 7. Gong, Y., Wagner, M. J., Li, J. Z. & Schnitzer, M. J. Imaging neural spiking in brain tissue
708   using FRET-opsin protein voltage sensors. *Nature Communications* **5**, (2014).

709 8. Bando, Y., Grimm, C., Cornejo, V. H. & Yuste, R. Genetic voltage indicators. *BMC Biology*
710   vol. 17 (2019).

711 9. Lee, S. *et al.* Improving a genetically encoded voltage indicator by modifying the
712   cytoplasmic charge composition. *Scientific Reports* **7**, (2017).

713 10. Xu, Y., Zou, P. & Cohen, A. E. Voltage imaging with genetically encoded indicators.
714   *Current Opinion in Chemical Biology* **39**, (2017).

715 11. Kannan, M., Vasan, G. & Pieribone, V. A. Optimizing strategies for developing genetically
716   encoded voltage indicators. *Frontiers in Cellular Neuroscience* **13**, (2019).

717 12. Beck, C., Zhang, D. & Gong, Y. Enhanced genetically encoded voltage indicators advance
718   their applications in neuroscience. *Current Opinion in Biomedical Engineering* **12**, (2019).

719 13. Knöpfel, T. & Song, C. Optical voltage imaging in neurons: moving from technology
720   development to practical tool. *Nature Reviews Neuroscience* **20**, (2019).

721 14. Peng, L., Xu, Y. & Zou, P. Genetically-encoded voltage indicators. *Chinese Chemical
722   Letters* **28**, (2017).

723 15. Piatkevich, K. D. *et al.* A robotic multidimensional directed evolution approach applied to
724   fluorescent voltage reporters article. *Nature Chemical Biology* **14**, (2018).

725 16. Abdelfattah, A. S. *et al.* A general approach to engineer positive-going eFRET voltage
726   indicators. *Nature Communications* **11**, (2020).

727 17. Ma, Y., Bayguinov, P. O. & Jackson, M. B. Optical studies of action potential dynamics
728   with hVOS probes. *Current Opinion in Biomedical Engineering* **12**, (2019).

729   18.   Mertz, J. *Introduction to optical microscopy*. *Introduction to Optical Microscopy* (2019).
730   doi:10.1017/9781108552660.

731   19.   Wu, J. *et al.* Kilohertz two-photon fluorescence microscopy imaging of neural activity in
732   vivo. *Nature Methods* **17**, (2020).

733   20.   Mertz, J. Optical sectioning microscopy with planar or structured illumination. *Nature*
734   *Methods* **8**, (2011).

735   21.   Harris, K. D., Quiroga, R. Q., Freeman, J. & Smith, S. L. Improving data quality in neuronal
736   population recordings. *Nature Neuroscience* **19**, (2016).

737   22.   Lim, S. T., Antonucci, D. E., Scannevin, R. H. & Trimmer, J. S. A novel targeting signal for
738   proximal clustering of the Kv2.1 K+ channel in hippocampal neurons. *Neuron* **25**, (2000).

739   23.   Xiao, S., Tseng, H. A., Gritton, H., Han, X. & Mertz, J. Video-rate volumetric neuronal
740   imaging using 3D targeted illumination. *Scientific Reports* **8**, (2018).

741   24.   Ishimaru, A. *Wave propagation and scattering in random media*. *Wave Propagation and*
742   *Scattering in Random Media* (1999). doi:10.1109/9780470547045.

743   25.   Brivanlou, I. H., Dantzker, J. L. M., Stevens, C. F. & Callaway, E. M. Topographic specificity
744   of functional connections from hippocampal CA3 to CA1. *Proceedings of the National*
745   *Academy of Sciences of the United States of America* **101**, (2004).

746   26.   Helmchen, F. & Denk, W. Deep tissue two-photon microscopy. *Nature Methods* **2**,
747   (2005).

748   27.   Kazemipour, A. *et al.* Kilohertz frame-rate two-photon tomography. *Nature Methods* **16**,
749   (2019).

750   28.   Zhang, T. *et al.* Kilohertz two-photon brain imaging in awake mice. *Nature Methods* **16**,
751   (2019).

752   29.   Pnevmatikakis, E. A. & Giovannucci, A. NoRMCorre: An online algorithm for piecewise
753   rigid motion correction of calcium imaging data. *Journal of Neuroscience Methods* **291**,
754   (2017).

755   30.   Mohammed, A. I. *et al.* An integrative approach for analyzing hundreds of neurons in
756   task performing mice using wide-field calcium imaging. *Scientific Reports* **6**, (2016).

757   31.   Griffiths, V. A. *et al.* Real-time 3D movement correction for two-photon imaging in
758   behaving animals. *Nature Methods* **17**, (2020).

759   32.   Jacques, S. L. Optical properties of biological tissues: A review. *Physics in Medicine and*
760   *Biology* **58**, (2013).

761   33.   Stokseth, P. A. Properties of a defocused optical system. *Journal of the Optical Society of*
762   *America* **59**, (1969).

763   34.   Yaroslavsky, A. N. *et al.* Optical properties of selected native and coagulated human
764   brain tissues in vitro in the visible and near infrared spectral range. *Physics in Medicine*
765   *and Biology* **47**, (2002).

766

767